

# Heat Transfer through the Interface of Solids and Nanoconfined Gas

Reza Rabani <sup>a,\*</sup>, Ahmadreza Pischevar <sup>a</sup>

<sup>a</sup> *Department of Mechanical Engineering, Isfahan University of Technology, Isfahan 84156-83111, Iran*  
[reza.rabani@pd.iut.ac.ir](mailto:reza.rabani@pd.iut.ac.ir), [apishe@cc.iut.ac.ir](mailto:apishe@cc.iut.ac.ir)

**ABSTRACT:** In the past few decades, great efforts are devoted to studying heat transfer in nanoscale due to its importance in multiple technologies such as thermal control and sensing applications. Heat conduction through the nanoconfined gas medium differs from macroscopic predictions due to several reasons. The continuum assumption is broken down; the surface forces become prominent due to the large surface-to-volume ratio, the wall force field is more extended through the gas medium, and, finally, the gas molecules are accumulated nonuniformly on the solid surfaces. In this work, to better understand the combination of these phenomena on the heat conduction through the nanoconfined gas medium, we present a series of molecular dynamics simulations of argon gas confined between metals and silicon walls. The gas density is set so that gas experiences a wide range of Knudsen numbers from continuum to the free molecular regime. It is observed that the temperature distribution through the gas medium for all metallic walls can be represented by a unique profile for the same gas density in the middle of the channel. It is also shown that the intrinsic characteristics of the solid determine the gas density distribution near the walls and consequently in the bulk region, and gas atoms distribution controls the heat conduction through the gas medium. While the nanochannel walls have their most significant impact on the rarefied gas's density, temperature, pressure, and heat flux, the pressure and heat flux are converged toward a plateau as the gas becomes denser. Finally, we propose a new analytical formula for calculating the heat flux through the argon gas, which incorporates the wall effects on gas transport characteristics for the Knudsen number in the range of 0.05 to 20.

**KEYWORDS:** Rarefied Gas; Dense Gas; Transition Regime; Pressure; Heat Conduction

---

\* Email: [reza.rabani@pd.iut.ac.ir](mailto:reza.rabani@pd.iut.ac.ir) (R.Rabani)

## A. Introduction

Growing demand for a better understanding of energy exchange on the nanoscale level has arisen during the past decade as nanotechnology is becoming an increasingly important part of contemporary sciences. Energy transfer between solid and gas medium in different rarefaction levels at nanoscale attracts vast attention due to a broad range of scientific and engineering applications such as thermal diode [1–3], thermal switch [3–6], gas sensors [7–10], and energy harvesting applications [11–13]. Consequently, heat transfer across the interface of solid and gas is studied continuously during past years using analytical, experimental, and numerical approaches [14–23]. Surface adsorption of the molecules on the solid walls, extension of the wall force field in the adjacent layer, and breakdown of the continuum hypothesis are the primary factors that complicate the numerical analysis of the nanoconfined gas medium. However, due to tackling such phenomena at the atomistic level, recently, the molecular dynamics (MD) method is used extensively for studying heat transfer in nanoscales confined liquid [24–40] or gas medium [41–47].

The high surface-to-volume ratio of the confined fluid in nanochannels and nanoslit makes them the first candidate for mass and heat transfer in some special applications [48–54]. Besides the above-mentioned intrinsic complexities, the high computational cost of MD simulations for rarefied gas in the nanochannel compared to its liquid counterpart is another limiting factor. This problem originates from the fact that the simulation domain should extend one mean free path in the periodic directions. Hence, a larger simulation domain is required for the rarefied gas than the liquid domain [55]. The cold wall models such as Smart Wall Molecular Dynamics (SWMD) [55] and Virtual Wall Model (VWM) [56] have also been proposed to reduce computational costs for the MD simulation of confined gases. In cold wall models, wall atoms that do not interact with each other are frozen at their initial position, and only their interactions with the gas atoms are considered in the MD simulation. Therefore, the computational time is decreased considerably.

A significant variation in the gas density and velocity was observed in the near-wall region when considering these cold wall models for the shear and force-driven nanochannel gas flow. The wall force field and its direct effect on increasing the gas atoms' residence time in such a region are responsible for this behavior [57,58]. Meanwhile, the equilibrium simulations showed

an anisotropic shear and normal stresses in the near-wall gas layer [59]. They also showed the role of the gas–wall interaction parameter and the Knudsen number ( $Kn$ ), which is defined as the ratio of the mean free path ( $\lambda$ ) to the characteristics nanochannel length scale ( $l$ ), in the transport phenomena in the bulk and near-wall region [60–62]. In addition, calculations showed that the gas–wall interaction energy characterized the surface adsorption of gas molecules [63]. Although many investigations well studied the hydrodynamics of confined gas in the nanochannels, less attention has been given to the thermal transport aspect of such configuration. Especially the rarefied gas case is less explored due to the cold wall models' limitation and the high computational cost of real wall MD simulation.

Recently, heat conduction characteristics of the nanoconfined gas medium were studied thoroughly using the interactive thermal wall model (ITWM) [64]. Generally, the following phenomena were observed for heat conduction between two parallel walls:

1. Depending on the physical characteristics of the solid and gas atoms, the interfacial and wall force field region thermal conductance could form a considerable portion of the total thermal resistance of the gas, even for near micrometer-sized channels [65–67].
2. While the induced heat flux decreased as the walls become stiffer, increasing the solid-gas interaction energy enhanced it toward a plateau. In addition, an approximately bell-shaped type curve for induced heat flux was observed as the solid atoms became heavier [68].
3. The wall force field creates one peak in the distribution of the gas atoms in 1 nm from each wall while decreasing the wall temperature for the dense gas medium can extend this region and create the second peak [66].
4. The wall temperature can intensify or reduce the density increment in the wall force field region for the cold and hot wall, respectively, by modifying gas residence time in the wall force field region [69,70].
5. When the gas is dense, the heat transport mechanism is purely diffusive. However, for the rarefied gas case, the heat transfer mechanism is a combination of ballistic mechanism in the bulk region and diffusive mechanism in the wall force field region[66].

6. The number of absorbed gas on the wall is found to be a function of wall temperature and solid-gas interaction energy [66,67].
7. The gas medium's kinetic stress, particle-particle virial, and surface-particle virial are affected by the gas density, wall temperature, and induced heat flux. As the gas becomes hotter, the normal stress distribution increases accordingly due to the increment in the kinetic stress, which dominates the bulk region. Near the hot wall, the surface-particle and particle-particle virial attenuated, while near the cold wall, these virials are intensified [71].

These observations were obtained based on a series of parametric studies in which one parameter was changed while the other parameters are kept constant. However, for the real wall in nanochannels, the dominating parameters such as wall stiffness, wall atom mass, and solid-gas interaction energy change simultaneously based on the wall material. Therefore, the phenomena mentioned above might change accordingly. In this study, to have a better understanding of the heat transfer characteristics of the nanoconfined gas domain, Silver (Ag), Aluminum (Al), Gold (Au), Copper (Cu), Platinum (Pt), and Silicon (Si) are considered as the wall materials and argon considered as the gas medium. The gas density has been changed while the channel height is kept constant at  $5.4\text{ nm}$ , so we could simulate a wide range of gas rarefaction from the continuum to free molecular regimes. This study enables us to estimate the combined effect of metal and nonmetal wall material and the gas density on the heat transfer characteristics of the nanoconfined gas domain.

## **B. Computational Model**

Simulations are performed using the open-source software LAMMPS (Large-Scale Atomic/Molecular Massively Parallel Simulator) [72]. A schematic sketch of the simulation domain for two different levels of gas rarefaction is shown in Fig. 1. In the axial ( $x$ ) and lateral ( $z$ ) directions, periodic boundary conditions are applied. Meanwhile,  $350\text{ K}$  and  $300\text{ K}$  are assigned to the bottom (hot) and top (cold) wall, respectively. In order to make sure that our data is independent of the simulation domain size, it is extends at least for one mean free path in the periodic directions [55]. To model the van der Waals interactions between gas-gas and gas-wall atoms, the truncated (6–12) Lennard–Jones (L–J) potential is used

$$\phi(r) = 4\varepsilon \left( \left( \left( \frac{\sigma}{r_{ij}} \right)^{12} - \left( \frac{\sigma}{r_{ij}} \right)^6 \right) - \left( \left( \frac{\sigma}{r_c} \right)^{12} - \left( \frac{\sigma}{r_c} \right)^6 \right) \right), \quad (1)$$

where  $r_c$  is the cutoff distance,  $r_{ij}$  is the interatomic distance, and  $\phi(r_c)$  is the value of the interatomic potential at  $r = r_c$ . The molecular diameter is  $\sigma = 0.3405$  nm, the depth of the potential well for argon is  $\varepsilon = 1.65 \times 10^{-21}$  J, and the mass of an argon atom is  $m = 6.63 \times 10^{-26}$  kg. Because the L-J potential is negligible at a large molecular distance, the cut-off radius is commonly set to  $r_c = 2.7$  nm and 1.08 nm for the dense and dilute gas medium, respectively [59]. The interaction parameters between wall and gas atoms are listed in Table 1, which is obtained based on the Lorentz-Berthelot (L-B) mixing rules for interaction strength, i.e.,  $\varepsilon_{solid-gas} = \sqrt{\varepsilon_{solid-solid} \times \varepsilon_{gas-gas}}$ . The embedded atom method (EAM) was used to model the metallic wall-wall interactions, which is a many-body interaction potential and works very well for FCC metallic structures [73]. Calculating the embedding energy as a function of the atomic electron density enables this method to predict a metallic structure's total energy accurately. Meanwhile, the Si-Si interactions were calculated using the Stillinger–Webber (SW) potential, which applies two-body terms for the pairwise interactions with additional many-body terms to stabilize the structure [74].

Newton's second law determined the motion of the gas and wall atoms by applying a velocity Verlet time integration algorithm [75]. The NVE ensemble is adopted in all simulations, and the LANGEVIN thermostat sets the desired temperature at the wall. Therefore, the thermostat is not applied to the gas when heat is appropriately transferred through the walls. The Maxwell–Boltzmann velocity distribution with the mean temperature of 325 K is used to initialize the argon gas and wall atoms at the initial state of the simulations. While a timestep of 4 fs is used in all simulations, smaller timesteps were also tested and had no significant effect on the results. The thermal equilibrium is reached when the initial particle distribution evolved for  $n_{init}$  timesteps. Then, the temperature is set to 350 K and 300 K for the bottom and the top wall, respectively, and the system is allowed to relax towards the expected temperature in  $n_{ssc}$  timesteps. Finally, additional  $n_{ave}$  timesteps are performed before the microscopic quantities are averaged to obtain the macroscopic properties.

The  $n_{init}$ ,  $n_{ssc}$  and  $n_{ave}$  for the rarefied gas medium are considered 5, 10, and  $20 \times 10^6$  timesteps, respectively, while for the dense gas medium 5, 10, and  $20 \times 10^5$  timesteps are performed. Longer time averaging is also performed in all cases to confirm the convergence of calculated quantities. Notable to say that the reported macroscopic amounts in this study are the average over four and eight different simulations for dense and rarefied gas medium, respectively, where the random generator number for the initial gas atoms distribution has been changed. The channel height is determined from the centerlines of the first layer of wall atoms at the top and bottom surfaces. The computational domain is divided into bins of approximately 0.054 nm and 0.108 nm for the density and temperature, respectively, perpendicular to the walls (y) direction.

We calculate the gas pressure in the middle of the channel as [59]

$$P = (S_{xx} + S_{yy} + S_{zz})/3, \quad (2)$$

where  $S_{xx}$ ,  $S_{yy}$  and  $S_{zz}$  are the normal stress components in  $x$ ,  $y$ , and  $z$  directions, respectively, and are calculated as

$$S_{kl} = \frac{1}{V} \left( \sum_{i=1} m_i (V_i^k - \bar{V}_i^k)(V_i^l - \bar{V}_i^l) + \frac{1}{2} (\sum_{i,j} r_{ij}^k) f_{ij}^l \right), \quad (3)$$

where  $k$  and  $l$  are the axes of the Cartesian coordinate system. In addition,  $\bar{V}_i^k$  and  $\bar{V}_i^l$  are the local average streaming velocities at the location of particle  $i$  in  $k$  and  $l$  directions, respectively, and  $V_i^k$  and  $V_i^l$  are peculiar velocity components in  $k$  and  $l$  directions. While  $f_{ij}^l$  is the  $l^{\text{th}}$  component of the force exerted on the atom  $i$  from the atom  $j$ ,  $r_{ij}^k$  is  $k^{\text{th}}$  component of the relative distance between particles  $i$  and  $j$ .

The Irving–Kirkwood (I–K) expression is applied to determine the induced heat flux vector through the gas domain [76,77]:

$$J_l = \frac{1}{\text{Vol}} \left\langle \sum_i V_l^i E_{tot}^i + \frac{1}{2} \sum_{i,j} r_l^{ij} (f^{ij} \cdot V^i) \right\rangle, \quad (4)$$

$$E_{tot}^i = \frac{1}{2} m^i \left( (V_x^i)^2 + (V_y^i)^2 + (V_z^i)^2 \right) + \phi^i, \quad (5)$$

where the summation is performed over all gas atoms. Considering  $l$  as the axes of the cartesian coordinate system,  $V_l^i$  is the velocity component of particle  $i$  in the  $l$ -direction. In addition,  $E_{tot}^i$  is the total energy, and  $\phi^i$  is the potential energy of particle  $i$ , which is calculated using Equations (5) and (1), respectively, and  $r_l^{ij}$  is the distance vector between particle  $i$  and  $j$ . Furthermore,  $f^{ij}$  is the vector of intermolecular force applied to particle  $i$  by particle  $j$ , and  $V^i$  is the velocity vector.

### C. Result and Discussion

The simulations are performed for two different sets of physics. In the first set of simulations, we changed the number of the argon gas atoms in the simulation domain to obtain the same density for the gas in the middle of the channel for all different walls. The number of gas atoms absorbed on the walls is mainly affected by the solid-gas interaction energy, which is not the same for all wall materials. Therefore, the exact number of gas atoms leading to the desired density in the middle of the channel is found via a trial-and-error method for each wall material. For the rarefied gas medium, the density in the middle of the channel is set at  $2.15 \text{ kg/m}^3$  while for the dense gas case,  $215 \text{ kg/m}^3$  seems reasonable. From here on, we call this set of simulations the constant density case. The number of gas atoms in the simulation domain is kept constant for the second set of simulations, called the constant atom number case. For the second set of simulations, 10000, 30000, 60000, and 100000 gas atoms are considered in the simulation domain, which leads to distinct gas densities in the middle of the channel and consequently different heat conduction characteristics.

Figure 2 shows the gas density distribution across the channel height for different walls of the constant density case. It is interesting to notice in Fig. 2a that for the rarefied gas regime, a nanochannel with Pt wall requires 27825 gas atoms to reach the density of  $2.15 \text{ kg/m}^3$  in the middle of the channel. Surprisingly, the nanochannel with Si walls needs 1000 gas atoms only to have the same gas density in a similar position. Other metals require many gas atoms between these limiting conditions. The difference originates from the different gas/metal interaction strengths, as shown in Table 1. Higher interaction strength between gas/metal leads to a denser gas layer in the wall force field region, i.e.,  $1 \text{ nm}$  from each wall. As an example, for the Pt nanochannel, the maximum density near hot and cold walls are about  $1265$  and  $1560 \text{ kg/m}^3$ ,

respectively, while for the Si walls, they become 22 and  $35 \text{ kg/m}^3$ . Meanwhile, the ratio between maximum gas density in the wall force field region of the cold wall and the middle of the channel is approximately 725 and 16 for the Pt and Si channel, which shows that the selected materials cover a wide range of physical phenomena.

Interestingly, for all the metallic walls, the maximum gas density occurs at  $0.5 \text{ nm}$  from the solid wall surface. In contrast for the Si wall, the maximum gas density formed closer to the surface. It means that the gas atoms get closer to the Si walls compared with metallic ones. A closer look at the wall's physical characteristics should reveal the source of such differences. Table 2 shows the physical characteristics of the different materials. The solid stiffness,  $K_S$ , which appears as the spring constant in the Einstein model, is obtained for each material as follows [78,79]:

$$K_S = \frac{m_w K_B^2 T_E^2}{\bar{h}^2}, \quad (6)$$

$T_E$  is the Einstein temperature,  $m_w$  is the solid atom mass,  $K_B = 1.3806 \times 10^{-23} \text{ J/K}$  is the Boltzmann constant, and  $\bar{h}$  is the reduced Planck constant. Notably, the Einstein temperature is derived based on the Debye temperature of the wall materials at room temperature of  $298 \text{ K}$  [80,81]. Table 2 clearly shows that the Si wall has the highest stiffness compared to the metals. For the higher value of wall stiffness, the wall atoms oscillate with lower amplitudes ( $\sim 1/K_S$ ) around their equilibrium position [82,83] let the gas atoms come closer to the wall as shown in Fig. 2a for the silicon wall.

According to Fig. 2b, the same phenomena are observed for the dense gas condition of the constant density case. The density of  $215 \text{ kg/m}^3$  in the middle of Pt and Si channel is achieved by the most 89000 and the least 67000 number of gas atoms, respectively. While Cu and Pt have the highest gas densities in the wall force field region of the hot and cold walls around 1900 and  $2000 \text{ kg/m}^3$ , Si has the lowest around 1000 and  $1250 \text{ kg/m}^3$  near the hot and cold walls, respectively. On the other hand, the ratio between maximum gas density in the wall force field region of the cold wall and the middle of the channel is approximately 9 and 6 for Pt and Si walls. This ratio has decreased too much compared to the rarefied gas, as discussed above. This comparison reveals that while the wall force field still affects the distribution of the atoms in the



dense gas medium, its effects are much more pronounced for the rarefied condition. The reason behind such a phenomenon is that for very low-density gas conditions, a gas atom mainly interacts with the force fields of the wall atoms rather than neighboring gas atoms. Therefore, the wall force field almost controls the motion of gas atoms. As the gas becomes denser, the number of the neighboring gas atoms increased accordingly, and consequently, the contribution of the gas atoms force field enhances. Hence, in such a case, both solid wall and neighboring gas atoms force field are the parameters that determine the motion of gas atoms.

Figures 3a and 3b show the temperature distribution across the channel height for the rarefied and dense gas cases, respectively. Figure 3a clearly shows that the temperature profile of dilute gas for metallic walls consists of three distinct regions. These divisions are conducted exclusively in Fig. 4a. In the first region, called the absorbed gas layer and extended from 0.2 to 0.7 *nm* from the wall, the gas and the wall atoms are in the thermal equilibrium with the same temperature. The second region extends from 0.7 to 1.5 *nm* near each wall and is called the wall force field region. In this layer, a linear variation for the temperature profile is observed. Beyond 1.5 *nm* from the wall, the third bulk layer is observed, i.e., the region in the middle of the channel where the gas atoms do not feel the wall force field is almost in constant temperature. These distinct behaviors originate from the different heat transfer mechanisms of the gas domain in these regions [66]. In the wall force field region, the gas density is 300 to 1500 *kg/m<sup>3</sup>*, depending on the wall material and temperature, which provokes the diffusive heat transfer mechanism. For the bulk gas region, the density is 2.15 *kg/m<sup>3</sup>* for all the metals, leading to a ballistic heat transfer mechanism as the collision between the gas atoms in the middle of the channel is rare. Considering Fig. 3b, it is clear that, unlike the rarefied case, the temperature profile of dense gas shows two distinct regions for metallic walls. The first region is the same as the rarefied condition, i.e., absorbed gas layer, which extends from 0.2 to 0.7 *nm*, and the gas has the same temperature as the walls. The rest of the channel height can be considered the second region. A linear variation of the temperature between the top and bottom walls denotes the diffusive heat transfer mechanism dominates in this region.

Inspection of Figs. 3a and 3b reveal that for a channel with the Si walls, the gas temperature profile consists of two distinct regions for the rarefied gas and only one region for the dense gas.

As emphasized by Fig 4b, for the rarefied case, the absorbed gas layer region is diminished by the silicon wall from the temperature profile. Instead, the wall force field region extends from 0.2 to 1 nm in which a linear variation for the temperature profile is observed. The rest of the channel height is dominated by the bulk medium for which the constant temperature denotes the presence of ballistic heat conduction mechanism in this region. Meanwhile, for the dense gas case, a temperature jump of 4 K occurs between the gas and Si surface, and linear temperature distribution is also observed between the gas temperature adjacent to the hot and cold walls. In contrast to metallic walls for which the temperature distribution along the channel height can be expressed with a unique curve regardless of the material type, see Figs. 3a and 3b, the Si wall temperature profile behaves quite differently. Figs. 2a and 2b imply that besides the gas density distribution in the bulk region, the distribution of the gas atoms in the wall force field region is the other determinative parameter that characterizes the temperature distribution across the channel height.

Figure 5 shows the density profile along the channel height for the constant gas atom number case. Since the number of the gas atoms is kept constant, the gas density in the middle of the channel is not the same for the selected wall materials due to the different solid-gas interaction energy. It can be observed that from all four cases, the gas in the Pt and Cu nanochannels produce the highest gas density near each wall while the Si has the lowest density. Our observation is a direct consequence of stronger interaction between Pt/Cu and the gas atoms in comparison with Si as stated in Table 1. Since the total number of the gas atoms is constant in each simulation, as expected the lowest gas density in the middle of the channel belongs to the Pt and Cu nanochannels and the highest one belongs to the Si nanochannel.

Considering the gas density in the bulk region of the channel for the most dilute gas case in Fig. 5a, i.e., 10000 gas atoms, the gas density for the Pt and Cu nanochannels are approximately 0.06 and 0.36 kg/m<sup>3</sup>, respectively. Similarly, it is 22 kg/m<sup>3</sup> as it comes to the Si walls. Therefore, the bulk gas in Si nanochannel is approximately 360 and 60 times denser than that of Pt and Cu channels. On the other hand, for the densest gas medium in Fig. 5d, i.e., 100000 gas atoms, the bulk gas density for the Pt nanochannel is approximately 265 kg/m<sup>3</sup>, which changes to 350 kg/m<sup>3</sup> for the Si. Therefore, the bulk gas in Si nanochannel is only 1.32 times denser than

that of Pt. This analogy reveals that the effect of the wall material on the density distribution of the rarefied gas is much more pronounced than the dense ones, as observed earlier for the constant gas density case. It is interesting to notice in Fig. 5a that for the most dilute gas case and the metallic wall, the maximum gas density near the cold and hot walls is in the range of  $600\sim 850\text{ kg/m}^3$  and  $275\sim 350\text{ kg/m}^3$ , respectively, depending on the metal type. However, for the densest gas medium of Fig. 5d, the maximum gas density near the cold and hot walls changes in the range of  $1500\sim 2000\text{ kg/m}^3$  and  $1400\sim 1900\text{ kg/m}^3$ . The same trend is also observed for the Si nanochannel. The results notify that for the most dilute case, the gas near the cold wall is twice denser than that of the hot wall, while for the highest density case, it is somehow in the same order of magnitude. Therefore, it is deduced that the impact of wall temperature on the dilute gas is more significant than the dense gas.

Figure 6 shows the temperature distribution in the gas medium along the channel height for the constant number of gas atom cases. A gradual transition from a constant temperature to a linear temperature profile can be observed in the bulk region as the gas become denser. As the gas density varies in the bulk region, the unified gas temperature distribution in the rarefied condition for the metallic walls is not observed anymore, unlike the constant density gas case. However, as the number of gas atoms increases, the unified temperature profile for the metallic walls is formed as the difference between the gas density in the bulk region reduces, as discussed before. Meanwhile, the Si wall has a different temperature distribution regardless of the number of gas atoms. Moreover, a temperature jump occurs even for the densest case, i.e., 100000 gas atoms. Shi et al. [84] showed that in the nanoconfined liquid medium, the temperature could not be defined at some location in the liquid argon adjacent to the solid surface. However, we have shown here that for a wide range of gas density and physical characteristics of the wall, the temperature can be defined in any position across the channel height, as shown by Fig. 6. This difference refers to the single peak nature of the density distribution in the nanoconfined gas compared to the density layering phenomena in the liquid medium.

The gas pressure in the middle of the channel is calculated using equations (2) and (3) and depicted in Fig. 7. The bulk pressure is the same for the various wall material in the constant gas density case, as shown in Fig. 7a, and for the rarefied gas case, the bulk pressure is about  $150\text{ kPa}$

while for the dense gas medium, it is about 14 *MPa*. Fig. 7b shows the calculated pressure for the constant atom number case. For 10000 gas atoms, the Pt and Si walls have the lowest and highest gas pressure in the middle of the channel of 3.77 *kPa* and 1.54 *MPa* , respectively, which shows a notable difference. It is expectable since the lowest and highest gas density in the middle of the channel were produced by these wall materials, according to Fig. 5a. The pressure developed by the other metals is between these limiting ranges. However, by increasing the number of gas atoms to 100000, the lowest and highest values of pressure by the Pt and Si walls in the middle of the channel are in the same order of magnitude and are 18 and 24 *MPa* , respectively. The other metals lead to pressure around 20 *MPa* in the gas. This observation again proves that the wall force field has its highest effect on the rarefied gas condition.

Using equations (4) and (5), the induced heat flux in the simulation domain is also computed for rarefied and dense gas cases. Fig. 8a shows that for the rarefied gas, when the constant gas density case is considered, the highest and lowest induced heat flux is for Al and Si walls which are 4.00 and 3.36 *MW/m<sup>2</sup>* , respectively. The heat flux for the other metallic walls is in the range of 3.8 ~3.9 *MW/m<sup>2</sup>*. For the dense gas, the maximum and minimum induced heat flux again belong to the Al and Si walls and are in the order of 178 and 150 *MW/m<sup>2</sup>* , respectively, and 174 *MW/m<sup>2</sup>* for the other metals. We deduced from the results that as long as the gas density is kept constant at the middle of the channel, the heat flux is not significantly affected by the material type for all metallic walls. However, the estimation is lower for the Si wall. The slight difference in the calculated heat flux for the metallic walls can be assigned to the inexact implementation of the thermostat applied to the walls and its adjacent fluid layer [85–87]. In the current study, the wall temperature is monitored carefully during the simulations for all cases to see whether the thermostat produces the desired temperature on the walls. The results show that the wall temperature is set with a maximum deviation of 1 K to its predefined values.

The maximum deviation in the heat flux for the nanochannels with metallic wall considered here is for the Al for which the walls and its adjacent gas layer experiences a temperature of 301 and 351 *K*, as shown in Fig. 3. The observed deviation in the wall temperature leads to a slightly higher heat flux for the rarefied and the dense gas cases, as shown in Fig. 8a. However, the difference of Si wall heat flux with the that of the metallic walls is so remarkable that it cannot

be related to the applied thermostat. Actually, for the Si walls, the maximum gas density near each wall is much lower than its corresponding metallic walls, according to Fig. 2. Therefore, the number of collisions between the gas and the wall atoms declined, reducing the transferred heat flux and resulting in a temperature jump, as shown in Fig. 3.

As stated before, the solid/ gas atom mass ratio, solid /gas interaction energy, and solid stiffness are the key parameters that affect the gas density distribution near the surface and eventually modifies energy transfer at the solid/gas interface [67,68,82,83]. The values used for these parameters in our simulations are listed in Table 2. Interestingly, despite parameter differences, the heat flux through the rarefied and dense gas is approximately the same for all metallic walls, as shown in Fig. 3a. Again, the accumulation of the gas atoms in the wall force field can cause this observation. The number of gas atoms adjacent to the wall is increased so that the number of collisions between gas and solid atoms becomes independent of the parameters mentioned above. Therefore, the absorbed gas on the wall reaches thermal equilibrium with the wall, as shown by Fig. 3.

Figure 8b shows the heat flux for the constant number of gas atom cases. Here, for the dilute gases, the extreme cases devote to Pt walls with a heat flux of  $0.112 \text{ MW}/\text{m}^2$ , and the Si walls with  $28.6 \text{ MW}/\text{m}^2$ . Such extraordinary difference originates from the different gas density distribution in the middle of the channel, as shown in Fig. 5a. As the number of gas atoms increases to the densest case, Pt and Al induce the lowest and highest heat flux of 203 and  $232 \text{ MW}/\text{m}^2$  through the gas domain. However, such huge differences disappeared, and the induced heat flux for all wall materials is converged toward a plateau between these limiting conditions.

Our discussion of induced heat flux is based on the gas density in the middle and near the channel walls so far. However, it is of practical use to reshape the obtained results for the heat flux in terms of the gas Knudsen number in the middle of the channel. Therefore, the calculated heat flux for both sets of simulations is rearranged in Fig. 9 based on their corresponding Knudsen number. Such arrangement helps us introducing a new correlation for the heat flux in the nanochannels for a wide range of Knudsen numbers between 0.05 to 20, which covers the whole transition regime in addition to some part of the continuum and free molecular regimes.

Equation (7) represents an analytical formula for the calculation of the induced heat flux through the gas domain in the transition regime with thermal conductivity of  $K$ , between two parallel surfaces at the temperature of  $T_1$  and  $T_2$  in the form of [88]:

$$q'' = \frac{K(T_1 - T_2)}{l \left( 1 + \frac{2 - \alpha}{\alpha} \frac{9\gamma - 5}{\gamma + 1} \sqrt{\frac{T_{m,FM}}{T_{m,DF}}} Kn \right)}, \quad (7)$$

in which  $\alpha$  denotes the energy accommodation coefficient,  $l$  is the distance between the surfaces,  $\gamma$  is the gas heat capacity ratio defined as  $C_p/C_v$ , and  $T_{m,DF} \sim T_{m,FM} \sim (T_1 + T_2)/2$  when the temperature difference between the surfaces is smaller than the temperature of the cooler ones, as we have in our study. This equation is derived analytically in which the effect of the wall force field in the density distribution and its corresponding impact on the induced heat flux is absent. By fitting this equation into our current data, we can incorporate the effect of the wall force field into the heat flux correlation for the nanochannels. For the argon as working media,  $\gamma$  equals 1.667 at 300 K, and the thermal conductivity  $K$  is estimated in terms of gas density by the semi-empirical equation of Lemmon and Jacobsen  $0.027\rho + 17.8$  [84].

Experimental investigation shows that  $\alpha$  for the argon gas interacting with metallic and silicon walls is about 0.9~0.95 for the ordinary surface without any special treatment. It was also shown that for a cleaner surface with argon-plasma treatment, these values are decreased by 0.05 [85]. More reduction in  $\alpha$  might occur for a much cleaner surface, which is hard to achieve [91]. Actually, in practical application, surface roughness and contamination, such as absorbed gas atoms on the solid surface, enhance the value of  $\alpha$  toward one [86]. It is also shown that using the L-B mixing rule to calculate the solid-gas interaction energy, as used in the current study, usually leads to  $\alpha \sim 1$  which is a good approximation for the practical application. Therefore, assuming  $\alpha = 1$  for the solid-gas interactions, equation (7) can be rewritten as follows:

$$q'' = \frac{0.27(\chi\rho) + 178}{1 + 3.75(\beta Kn)}, \quad (8)$$

Where  $\chi$  and  $\beta$  are introduced to fit the numerical data. Substituting the gas density by  $\rho = 23.85/Kn$  in equation (8), as proposed for the argon gas [66], the heat flux can be expressed in terms of gas Knudsen number as:

$$q'' = \frac{178 + \frac{8.85}{Kn}}{1 + 4.54Kn}, \quad (9)$$

For parameters  $\chi = 1.375$  and  $\beta = 1.21$ , equation (9) is compared to numerical data in Fig. 9.

## Conclusions

Heat conduction through the nanoconfined argon gas medium has been studied thoroughly using molecular dynamics simulation. The Ag, Al, Au, Cu, Pt and, Si are considered the wall materials in a 5.4 nm channel height. The gas density has been changed while the channel height is kept constant, so a wide range of Knudsen numbers from continuum to free molecular regime has been studied. The following phenomena are observed:

- The density distribution along the channel height is mainly affected by the physical characteristics of the wall when the gas is rarefied. Generally, the density peak near the silicon wall is weaker than the metallic ones, forming closer to the wall.
- The metallic walls lead to a unified temperature profile through the gas when the gas density distribution in the middle of the channel is the same. The temperature profile for the silicon wall deviates from the metallic one even if it satisfies the density condition.
- The temperature profile for the rarefied gas in the metallic nanochannel consists of three distinct regions: the absorbed gas layer, which is in thermal equilibrium with the adjacent wall, the wall force field region in which the diffusive transport mechanism is dominated, and the bulk region with a ballistic transport property. The absorbed gas layer and bulk region with diffusive nature are only observed for the dense gas case.
- The temperature profile shows a diffusive transport mechanism in the wall force field region in silicon nanochannels filled with a dilute gas. The ballistic transport mechanism dominates the bulk region. In contrast, a temperature jump can be observed on the walls. Meanwhile, for the dense gas, a linear temperature profile is only observed.
- The effect of wall material on the pressure and heat flux through the gas domain is much more pronounced as the gas is rarefied. The pressure and heat flux converge toward a plateau as the gas becomes denser, and the wall material type loses importance.

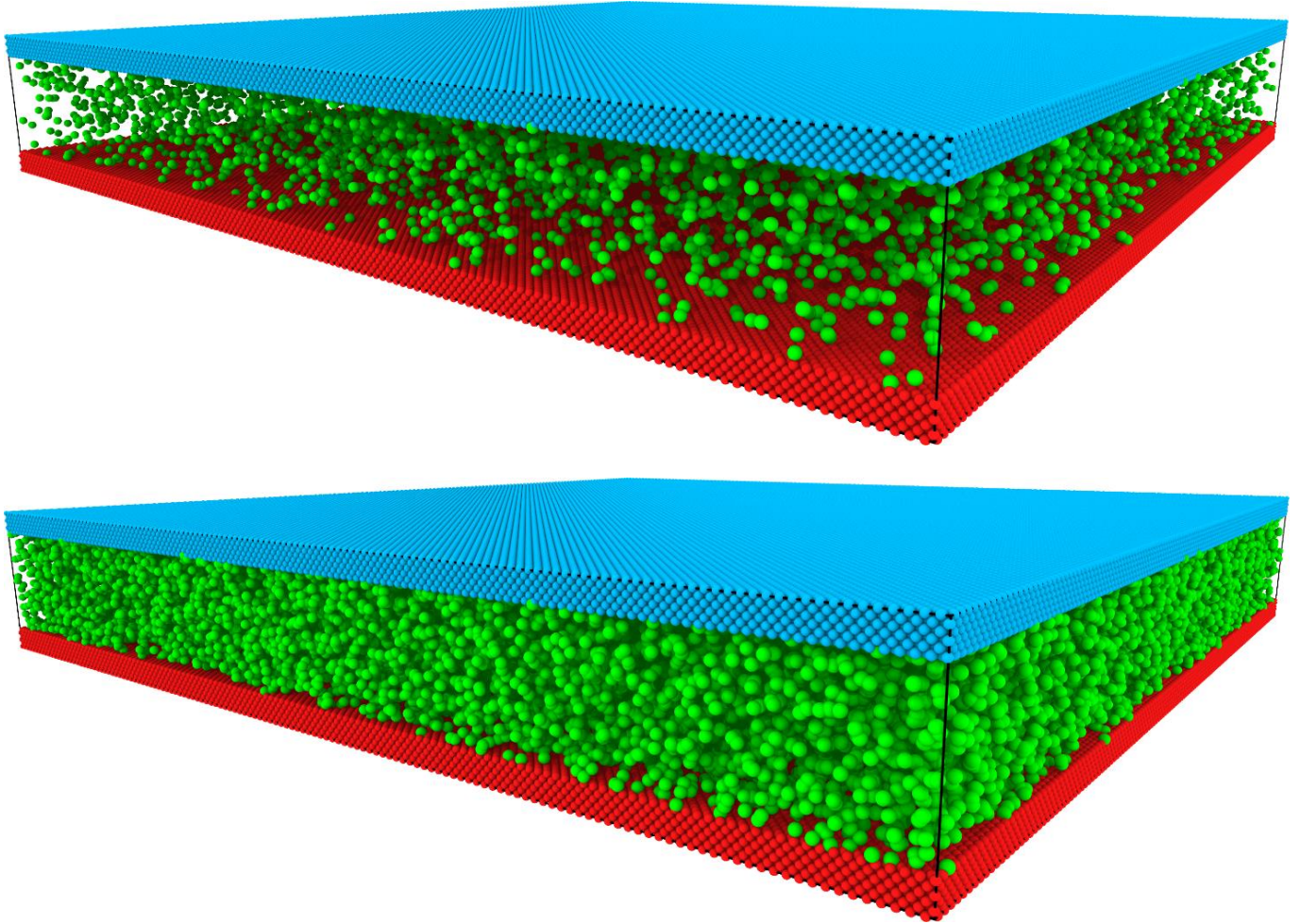


**Fig. 1.** Snapshot of the simulation domain for dilute (**top**) and dense (**bottom**) gas medium between top (*Cold* – 300 K) and bottom (*Hot* – 350 K) walls



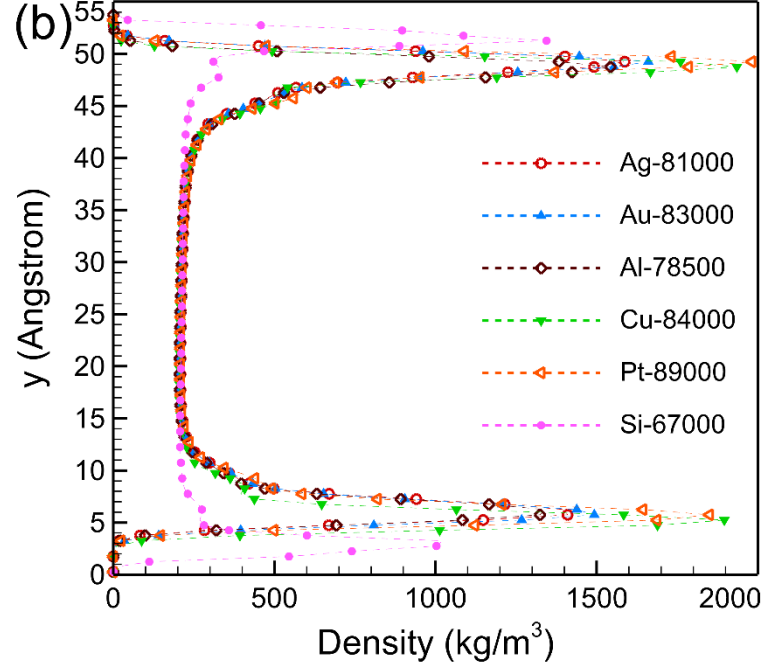
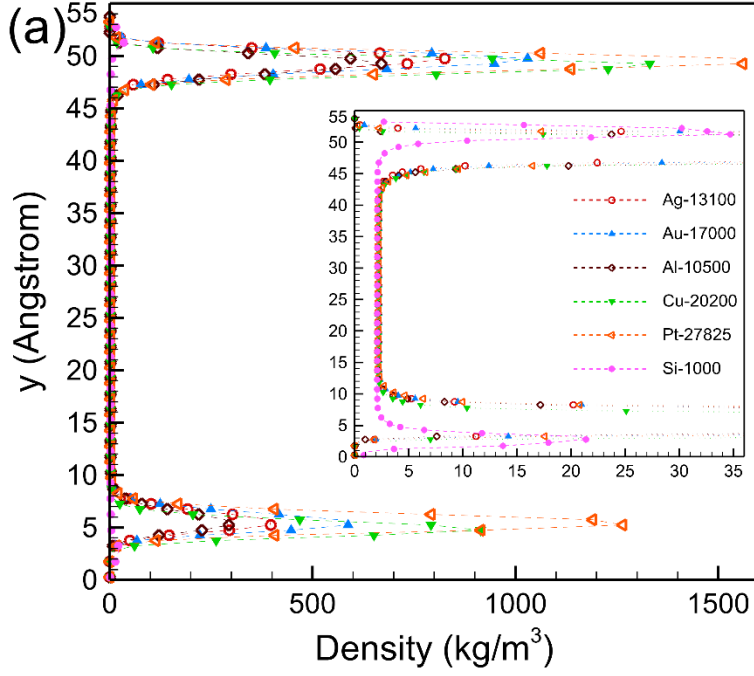


**Fig. 2.** Density distribution in the simulation domain for dilute (a) and dense (b) gas medium for constant density case

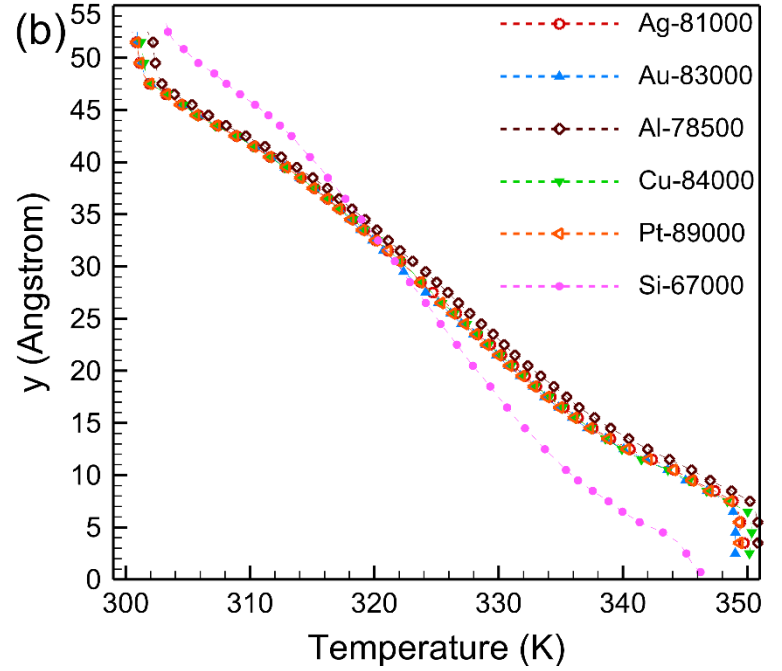
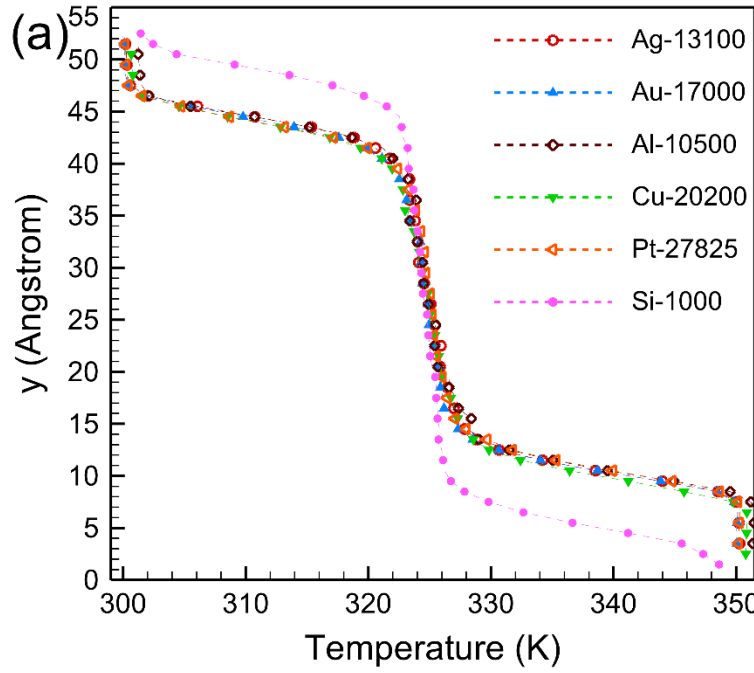


**Fig. 3.** Temperature distribution in the simulation domain for dilute (a) and dense (b) gas medium for constant density case

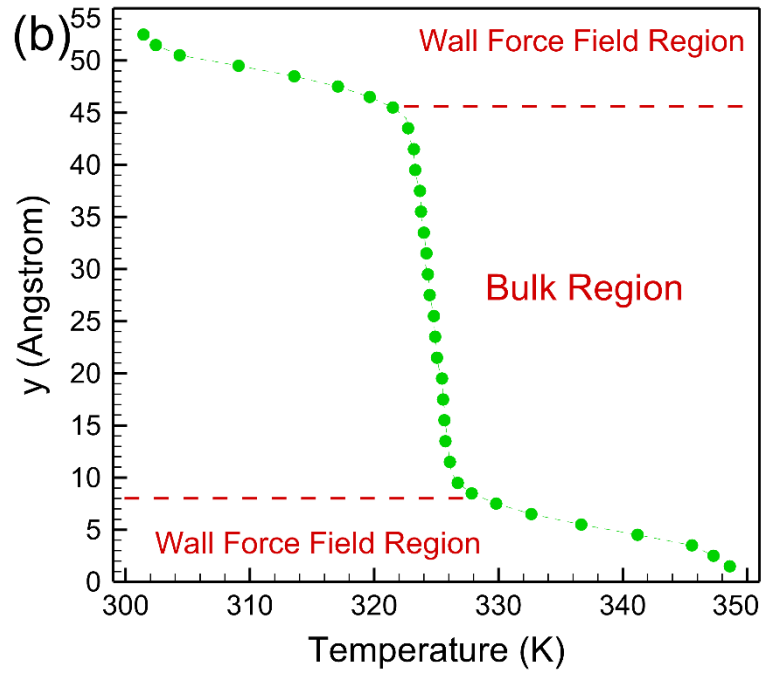
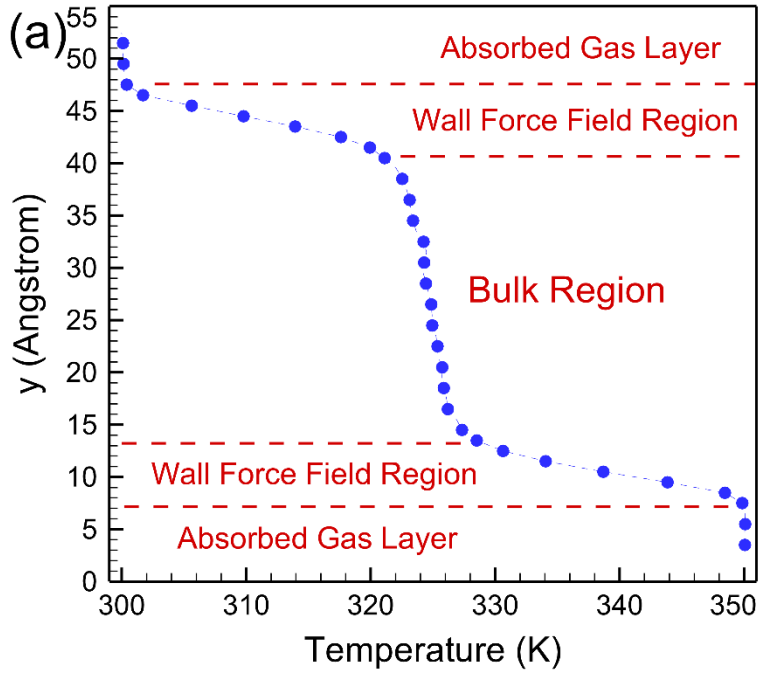


**Fig. 4.** Schematic division of the channel height based on the transport mechanism for metallic **(a)** and Silicon **(b)** wall for constant density case of the rarefied gas

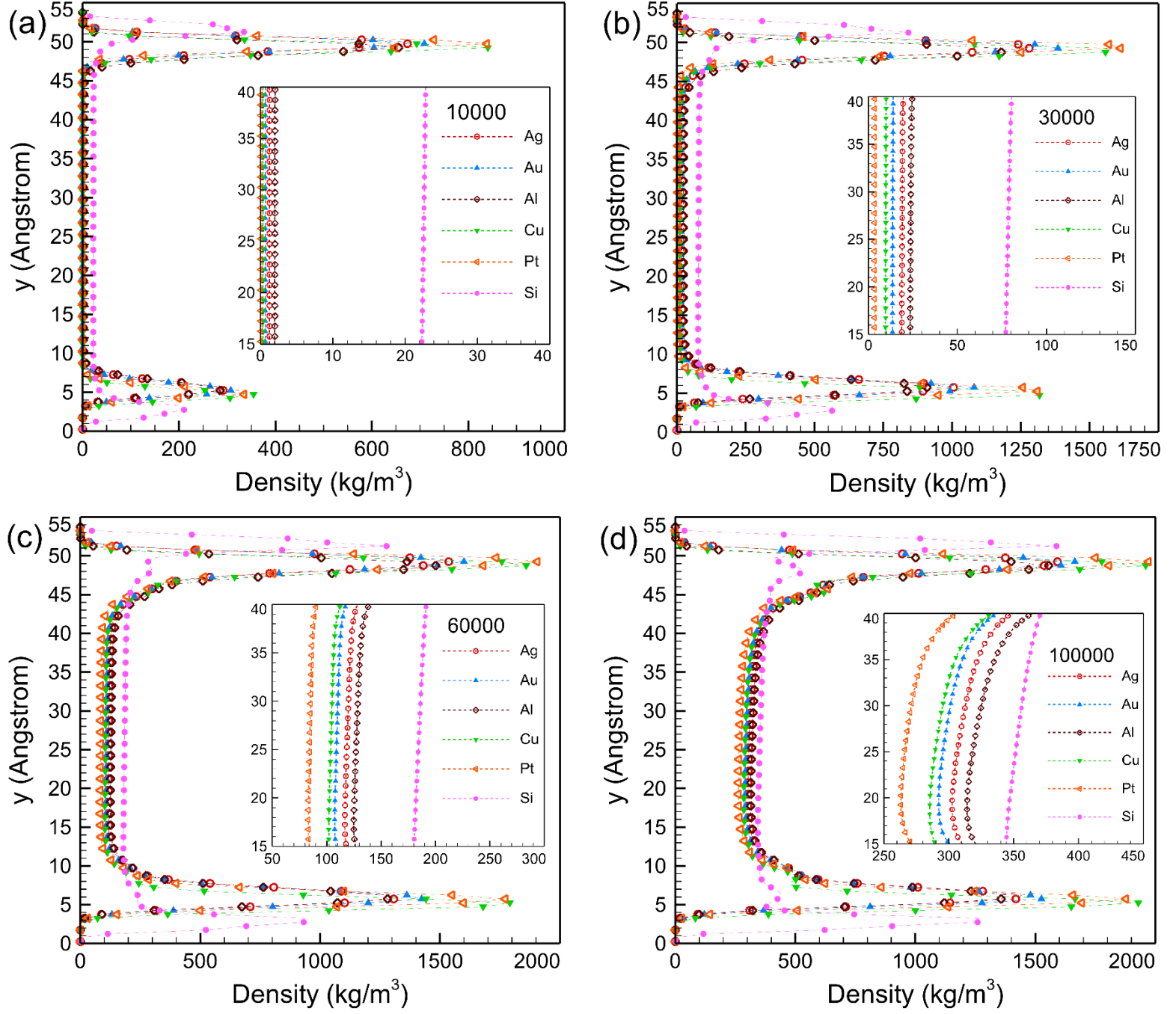


**Fig. 5.** Density distribution along the channel height for 10000 (a), 30000 (b), 60000 (c), and 100000 (d) gas atoms for constant gas atom number in the simulation domain

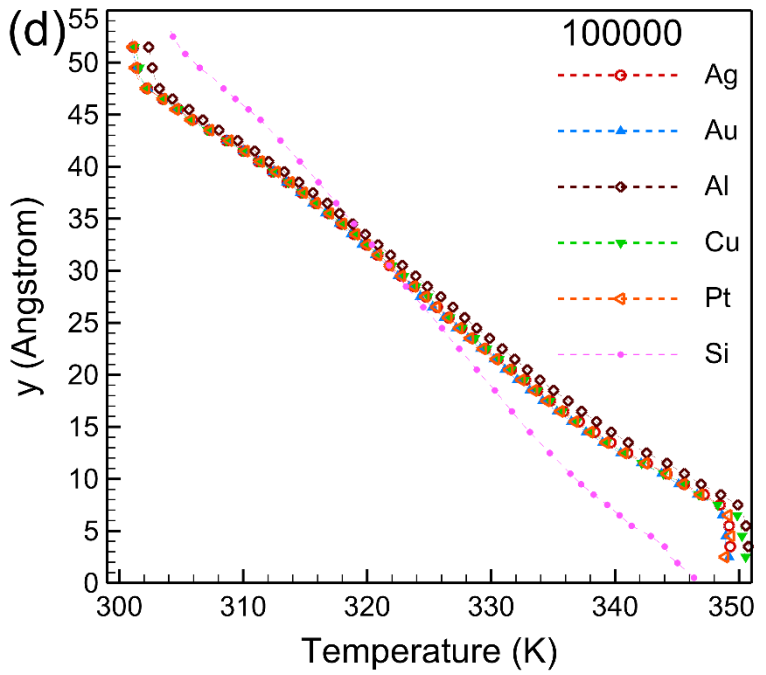
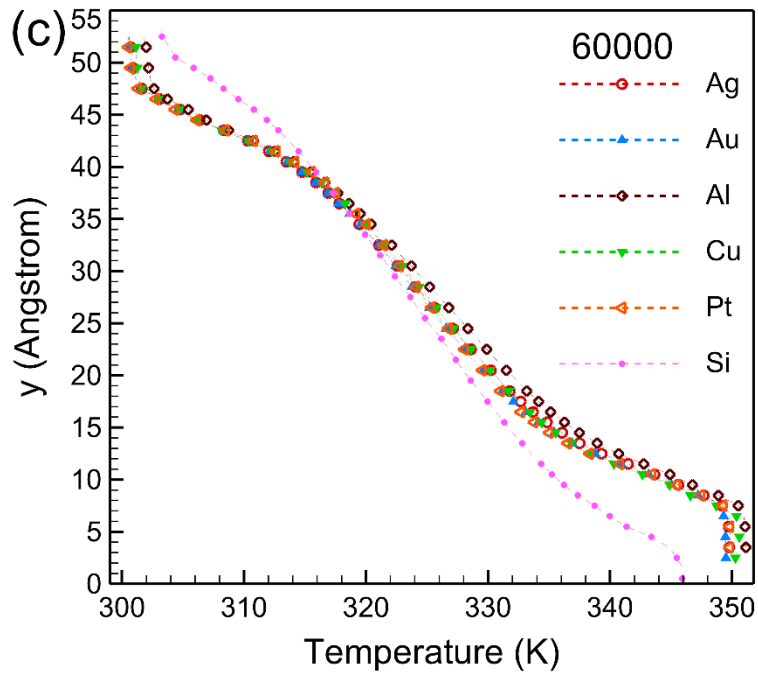
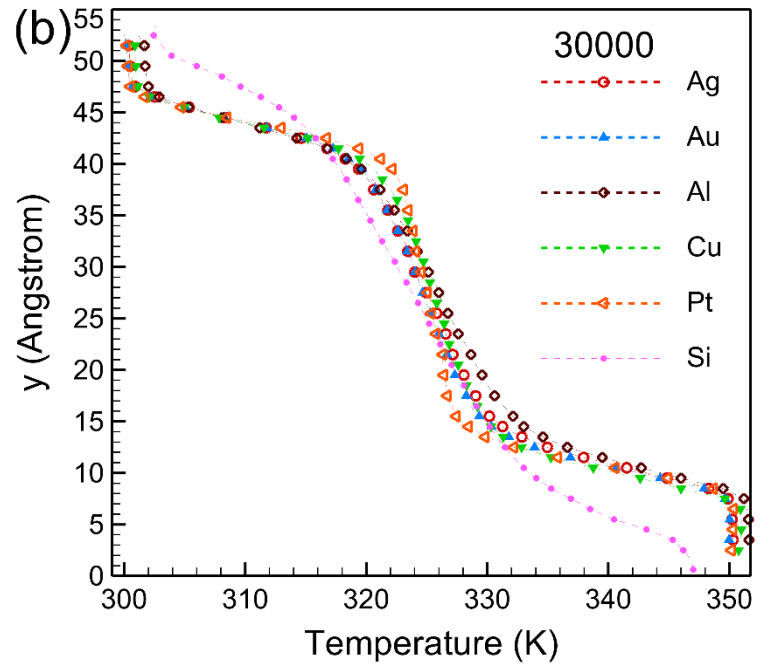
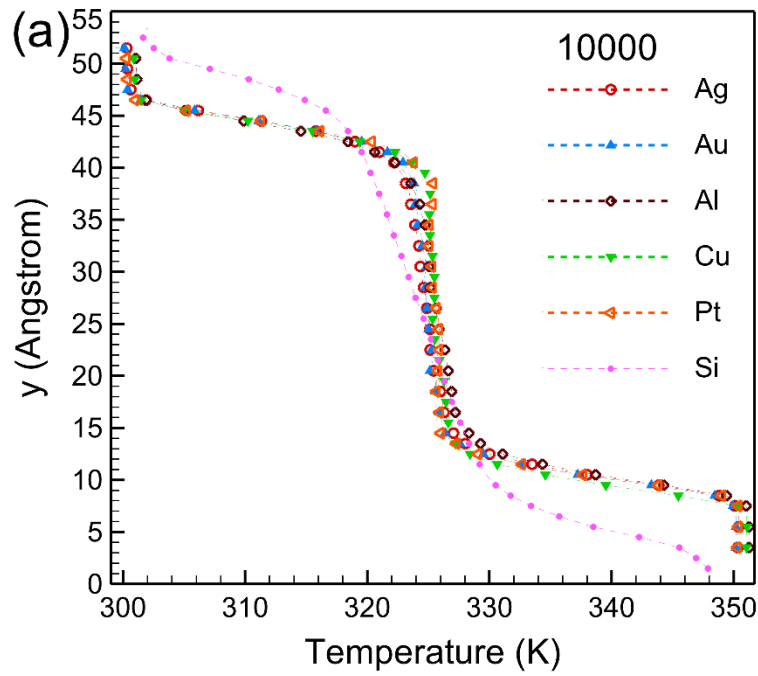


**Fig. 6.** Temperature distribution along the channel height for 10000 (a), 30000 (b), 60000 (c), and 100000 (d) gas atoms for constant gas atom number in the simulation domain

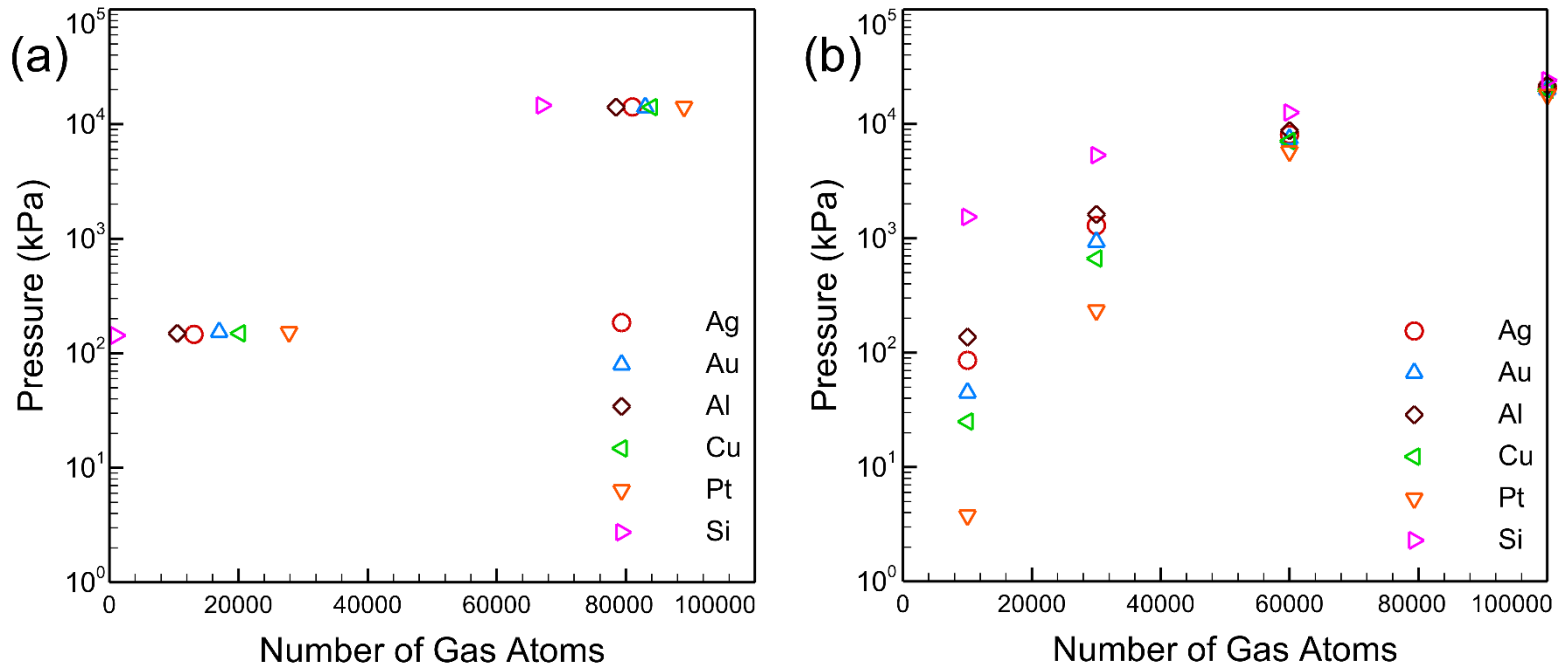


**Fig. 7.** Calculated pressure in the middle of the channel height for constant density **(a)** and constant number of gas atoms **(b)** cases

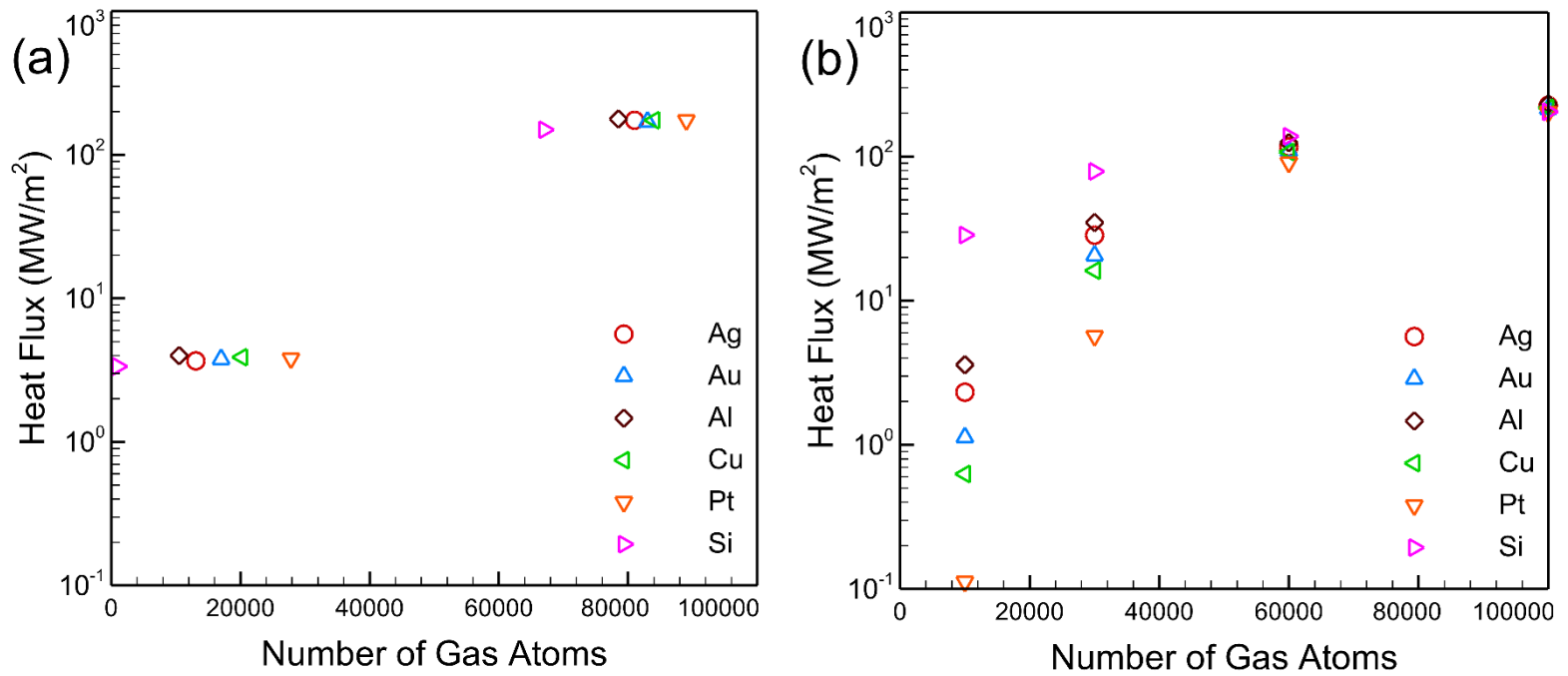


**Fig. 8.** Calculated heat flux in the middle of the channel height for constant density **(a)** and constant number of gas atoms **(b)** cases

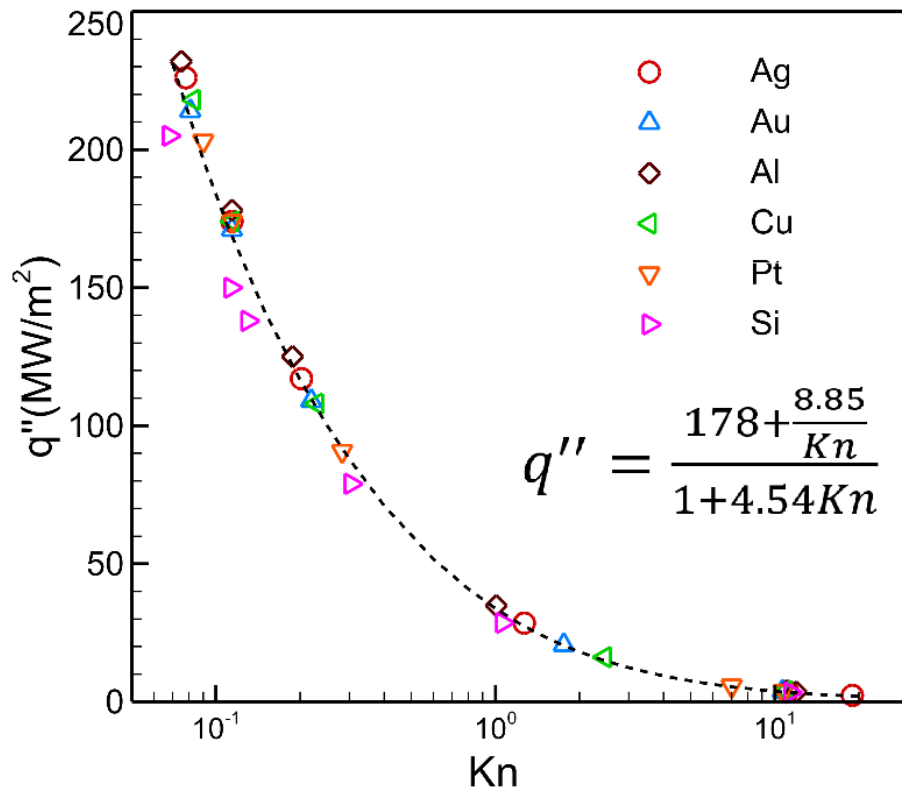


**Fig. 9.** Variation of induced heat flux as a function of Knudsen number for different wall materials and its corresponding analytical fitted curve

**Table 1** Interaction parameters in the simulation of the gas and wall atoms [87]

	$\sigma$ (nm)	$\epsilon_{solid-gas}$ (J)	$\frac{\epsilon_{solid-gas}}{\epsilon_{gas-gas}}$
<i>Ag</i> [87]	0.2955	$7.25 \times 10^{-21}$	4.37
<i>Au</i> [87]	0.295	$7.8 \times 10^{-21}$	4.7
<i>Al</i> [87]	0.293	$6.8 \times 10^{-21}$	4.1
<i>Cu</i> [87]	0.2616	$7.37 \times 10^{-21}$	4.44
<i>Pt</i> [87]	0.2845	$9.5 \times 10^{-21}$	5.7
<i>Si</i> [88–90]	0.338	$2.56 \times 10^{-21}$	1.55

**Table 2** Physical and calculated properties of the argon gas and solid wall

	$T_E$ (K)	$K_S$ (N/m)	$m_{atom}$ (Kg)	$\frac{m_{wall}}{m_{gas}}$	$\omega$ (Hz)
<i>Ag</i> [80,81]	172	90	$17.9 \times 10^{-26}$	2.7	2.24
<i>Au</i> [80,81]	131	96	$32.7 \times 10^{-26}$	4.93	1.71
<i>Al</i> [80,81]	317	77	$4.48 \times 10^{-26}$	0.68	4.15
<i>Cu</i> [80,81]	248	110	$10.5 \times 10^{-26}$	1.58	3.24
<i>Pt</i> [78,79]	180	180	$32.4 \times 10^{-26}$	4.89	2.36
<i>Si</i> [81]	558	248	$4.66 \times 10^{-26}$	0.703	7.29

## CONFLICT OF INTEREST

There are no conflicts to declare.

## ACKNOWLEDGMENTS

R.Rabani and A.Pishevar wish to thank the financial support of the Isfahan University of Technology.

## References

- [1] M.Y. Wong, C.Y. Tso, T.C. Ho, H.H. Lee, A review of state of the art thermal diodes and their potential applications, *Int. J. Heat Mass Transf.* 164 (2021) 120607. <https://doi.org/10.1016/j.ijheatmasstransfer.2020.120607>.
- [2] T. Avanessian, G. Hwang, Thermal diode in gas-filled nanogap with heterogeneous surfaces using nonequilibrium molecular dynamics simulation, *J. Appl. Phys.* 120 (2016) 165306. <https://doi.org/10.1063/1.4966599>.
- [3] T. Avanessian, G. Hwang, Adsorption and capillary transition in heterogeneous nanostructures using Grand Canonical Monte Carlo simulation, *Int. J. Heat Mass Transf.* 123 (2018) 879–887. <https://doi.org/10.1016/j.ijheatmasstransfer.2018.03.018>.
- [4] K. Klinar, T. Swoboda, M. Muñoz Rojo, A. Kitanovski, Fluidic and Mechanical Thermal Control Devices, *Adv. Electron. Mater.* 7 (2021) 2000623. <https://doi.org/10.1002/aelm.202000623>.
- [5] T. Avanessian, G. Hwang, Thermal switch using controlled capillary transition in heterogeneous nanostructures, *Int. J. Heat Mass Transf.* 121 (2018) 127–136. <https://doi.org/10.1016/j.ijheatmasstransfer.2017.12.142>.
- [6] G. Wehmeyer, T. Yabuki, C. Monachon, J. Wu, C. Dames, Thermal diodes, regulators, and switches: Physical mechanisms and potential applications, *Appl. Phys. Rev.* 4 (2017) 041304. <https://doi.org/10.1063/1.5001072>.
- [7] J. Zhang, E. Strelcov, A. Kolmakov, Heat dissipation from suspended self-heated nanowires: Gas sensor prospective, *Nanotechnology.* 24 (2013) 444009. <https://doi.org/10.1088/0957-4484/24/44/444009>.
- [8] C. Fàbrega, O. Casals, F. Hernández-Ramírez, J.D. Prades, A review on efficient self-heating in nanowire sensors: Prospects for very-low power devices, *Sensors Actuators, B Chem.* 256 (2018) 797–811. <https://doi.org/10.1016/j.snb.2017.10.003>.
- [9] Y. Wang, L. Duan, Z. Deng, J. Liao, Electrically transduced gas sensors based on semiconducting metal oxide nanowires, *Sensors (Switzerland).* 20 (2020) 1–41. <https://doi.org/10.3390/s20236781>.
- [10] H. Yamaguchi, M.T. Ho, Y. Matsuda, T. Niimi, I. Graur, Conductive heat transfer in a gas confined between two concentric spheres: From free-molecular to continuum flow regime, *Int. J. Heat Mass Transf.* 108 (2017) 1527–1534. <https://doi.org/10.1016/j.ijheatmasstransfer.2016.12.100>.
- [11] R. McCarty, D. Monaghan, K.P. Hallinan, B. Sanders, Experimental verification of thermal switch effectiveness in thermoelectric energy harvesting, *J. Thermophys. Heat Transf.* 21 (2007) 505–511. <https://doi.org/10.2514/1.27842>.



- [12] X. Gou, H. Ping, Q. Ou, H. Xiao, S. Qing, A novel thermoelectric generation system with thermal switch, *Appl. Energy*. 160 (2015) 843–852.  
<https://doi.org/10.1016/j.apenergy.2014.11.049>.
- [13] S. Cui, J. Fu, M. Guo, Z. Zhao, C. Sun, Y. Wang, Diffusion of High-Temperature and High-Pressure CH<sub>4</sub> Gas in SiO<sub>2</sub> Nanochannels, *Front. Energy Res.* 9 (2021) 175.  
<https://doi.org/10.3389/fenrg.2021.667640>.
- [14] W.D. Zhou, B. Liu, S.K. Yu, W. Hua, Rarefied-gas heat transfer in micro- and nanoscale Couette flows, *Phys. Rev. E - Stat. Nonlinear, Soft Matter Phys.* 81 (2010) 1–7.  
<https://doi.org/10.1103/PhysRevE.81.011204>.
- [15] S. V. Nedeia, A.J. Markvoort, A.A. van Steenhoven, P.A.J. Hilbers, Heat Transfer Predictions for Micro-/Nanochannels at the Atomistic Level Using Combined Molecular Dynamics and Monte Carlo Techniques, *J. Heat Transfer*. 131 (2009) 033104.  
<https://doi.org/10.1115/1.3056592>.
- [16] M. Kasprzak, M. Sledzinska, K. Zaleski, I. Iatsunskyi, F. Alzina, S. Volz, C.M. Sotomayor Torres, B. Graczykowski, High-temperature silicon thermal diode and switch, *Nano Energy*. 78 (2020) 105261. <https://doi.org/10.1016/j.nanoen.2020.105261>.
- [17] B. Graczykowski, A. El Sachat, J.S. Reparaz, M. Sledzinska, M.R. Wagner, E. Chavez-Angel, Y. Wu, S. Volz, Y. Wu, F. Alzina, C.M. Sotomayor Torres, Thermal conductivity and air-mediated losses in periodic porous silicon membranes at high temperatures, *Nat. Commun.* 8 (2017) 1–9. <https://doi.org/10.1038/s41467-017-00115-4>.
- [18] T. Feng, A. Rai, D. Hun, S.S. Shrestha, Molecular dynamics simulations of energy accommodation between gases and polymers for ultra-low thermal conductivity insulation, *Int. J. Heat Mass Transf.* 164 (2021) 120459.  
<https://doi.org/10.1016/j.ijheatmasstransfer.2020.120459>.
- [19] M.T. Alam, A.P. Raghu, M.A. Haque, C. Muratore, A.A. Voevodin, Structural size and temperature dependence of solid to air heat transfer, *Int. J. Therm. Sci.* 73 (2013) 1–7.  
<https://doi.org/10.1016/j.ijthermalsci.2013.05.010>.
- [20] C. Cheng, W. Fan, J. Cao, S.G. Ryu, J. Ji, C.P. Grigoropoulos, J. Wu, Heat transfer across the interface between nanoscale solids and gas, *ACS Nano*. 5 (2011) 10102–10107.  
<https://doi.org/10.1021/nn204072n>.
- [21] J.S. Lee, K.W. Choi, J.Y. Yoo, M.S. Jo, J.B. Yoon, Realization of Nanolene: A Planar Array of Perfectly Aligned, Air-Suspended Nanowires, *Small*. 16 (2020) 1906845.  
<https://doi.org/10.1002/sml.201906845>.
- [22] Q. Sun, K.S. Choi, X. Mao, An analytical solution of convective heat transfer in microchannel or nanochannel, *Int. Commun. Heat Mass Transf.* 117 (2020) 104766.  
<https://doi.org/10.1016/j.icheatmasstransfer.2020.104766>.
- [23] S.Y. Docherty, M.K. Borg, D.A. Lockerby, J.M. Reese, Multiscale simulation of heat transfer in a rarefied gas, *Int. J. Heat Fluid Flow*. 50 (2014) 114–125.  
<https://doi.org/10.1016/j.ijheatfluidflow.2014.06.003>.
- [24] J. Vera, Y. Bayazitoglu, Temperature and heat flux dependence of thermal resistance of water/metal nanoparticle interfaces at sub-boiling temperatures, *Int. J. Heat Mass Transf.* 86 (2015) 433–442. <https://doi.org/10.1016/j.ijheatmasstransfer.2015.02.033>.
- [25] A.R. bin Saleman, H.K. Chilukoti, G. Kikugawa, M. Shibahara, T. Ohara, A molecular dynamics study on the thermal transport properties and the structure of the solid–liquid

- interfaces between face centered cubic (FCC) crystal planes of gold in contact with linear alkane liquids, *Int. J. Heat Mass Transf.* 105 (2017) 168–179.  
<https://doi.org/10.1016/j.ijheatmasstransfer.2016.09.069>.
- [26] M. Frank, M. Kio, D. Drikakis, L. Könözy, N. Asproulis, Mass and Stiffness Effects on Thermal Resistance at the Solid–Liquid Interface of Nanofluidic Channels, *J. Comput. Theor. Nanosci.* 15 (2018) 141–146. <https://doi.org/10.1166/jctn.2018.7066>.
- [27] L. Xue, P. Keblinski, S.R. Phillpot, S.U.S. Choi, J.A. Eastman, Effect of liquid layering at the liquid-solid interface on thermal transport, *Int. J. Heat Mass Transf.* 47 (2004) 4277–4284. <https://doi.org/10.1016/j.ijheatmasstransfer.2004.05.016>.
- [28] F. Sofos, T.E. Karakasidis, A. Liakopoulos, How wall properties control diffusion in grooved nanochannels: A molecular dynamics study, *Heat Mass Transf. Und Stoffuebertragung.* 49 (2013) 1081–1088. <https://doi.org/10.1007/s00231-013-1152-9>.
- [29] D.M. Huang, C. Cottin-Bizonne, C. Ybert, L. Bocquet, Ion-specific anomalous electrokinetic effects in hydrophobic nanochannels, *Phys. Rev. Lett.* 98 (2007) 177801. <https://doi.org/10.1103/PhysRevLett.98.177801>.
- [30] C. Sun, R. Zhou, Z. Zhao, B. Bai, Nano-Confined Fluid: What Can We Expect From It?, *J. Phys. Chem. Lett.* (2020) acs.jpcllett.0c00591. <https://doi.org/10.1021/acs.jpcllett.0c00591>.
- [31] M. Bagheri Motlagh, M. Kalteh, Investigating the wall effect on convective heat transfer in a nanochannel by molecular dynamics simulation, *Int. J. Therm. Sci.* 156 (2020) 106472. <https://doi.org/10.1016/j.ijthermalsci.2020.106472>.
- [32] H. Matsubara, G. Kikugawa, T. Ohara, Comparison of molecular heat transfer mechanisms between water and ammonia in the liquid states, *Int. J. Therm. Sci.* 161 (2021) 106762. <https://doi.org/10.1016/j.ijthermalsci.2020.106762>.
- [33] Z. Li, L. Cui, B. Li, X. Du, Enhanced heat conduction in molten salt containing nanoparticles: Insights from molecular dynamics, *Int. J. Heat Mass Transf.* 153 (2020) 119578. <https://doi.org/10.1016/j.ijheatmasstransfer.2020.119578>.
- [34] A. Mosavi, M. Zarringhalam, D. Toghraie, A. Rahmani, A. Karimipour, Boiling of Argon flow in a microchannel by considering the spherical geometry for roughness barriers using molecular dynamics simulation, *J. Mol. Liq.* 321 (2021) 114462. <https://doi.org/10.1016/j.molliq.2020.114462>.
- [35] F. Sofos, T.E. Karakasidis, A. Liakopoulos, Parameters affecting slip length at the nanoscale, *J. Comput. Theor. Nanosci.* 10 (2013) 648–650. <https://doi.org/10.1166/jctn.2013.2749>.
- [36] M. Rashedul Hasan, T. Quoc Vo, BoHung Kim, Manipulating thermal resistance at the solid–fluid interface through monolayer deposition, *RSC Adv.* 9 (2019) 4948–4956. <https://doi.org/10.1039/C8RA08390H>.
- [37] J. Al Hossain, B. Kim, Scale Effect on Simple Liquid Transport through a Nanoporous Graphene Membrane, *Langmuir.* (2021). <https://doi.org/10.1021/acs.langmuir.1c00643>.
- [38] K.E. Karim, B.H. Kim, First law of thermodynamics on the boundary for flow through a carbon nanotube, *Phys. Rev. E.* 103 (2021) 053115. <https://doi.org/10.1103/PhysRevE.103.053115>.
- [39] M.R. Hasan, B.H. Kim, Molecular transportation phenomena of simple liquids through a nanoporous graphene membrane, *Phys. Rev. E.* 102 (2020) 033110.

- <https://doi.org/10.1103/PhysRevE.102.033110>.
- [40] C. Jiang, X. Wang, Q. Liu, X. Wang, C. Ke, Investigation of the relationship between nanochannel width and mass transfer characteristics for dense methane nanofluidics, *Int. Commun. Heat Mass Transf.* 118 (2020) 104879. <https://doi.org/10.1016/J.ICHEATMASSTRANSFER.2020.104879>.
  - [41] Q. Sheng, L. Gibelli, J. Li, M.K. Borg, Y. Zhang, Dense gas flow simulations in ultra-tight confinement, *Phys. Fluids.* 32 (2020) 092003. <https://doi.org/10.1063/5.0019559>.
  - [42] T. Xiao, K. Xu, Q. Cai, T. Qian, An investigation of non-equilibrium heat transport in a gas system under external force field, *Int. J. Heat Mass Transf.* 126 (2018) 362–379. <https://doi.org/10.1016/J.IJHEATMASSTRANSFER.2018.05.035>.
  - [43] Z. Liang, W. Evans, T. Desai, P. Keblinski, Improvement of heat transfer efficiency at solid-gas interfaces by self-assembled monolayers, *Appl. Phys. Lett.* 102 (2013). <https://doi.org/10.1063/1.4792530>.
  - [44] Z. Liang, W. Evans, P. Keblinski, Equilibrium and nonequilibrium molecular dynamics simulations of thermal conductance at solid-gas interfaces, *Phys. Rev. E - Stat. Nonlinear, Soft Matter Phys.* 87 (2013). <https://doi.org/10.1103/PhysRevE.87.022119>.
  - [45] Z. Liang, P. Keblinski, Parametric studies of the thermal and momentum accommodation of monoatomic and diatomic gases on solid surfaces, *Int. J. Heat Mass Transf.* 78 (2014) 161–169. <https://doi.org/10.1016/j.ijheatmasstransfer.2014.06.038>.
  - [46] B.S. Day, J.R. Morris, Packing density and structure effects on energy-transfer dynamics in argon collisions with organic monolayers, *J. Chem. Phys.* 122 (2005). <https://doi.org/10.1063/1.1924693>.
  - [47] G.S. Hwang, M. Kaviani, Molecular dynamics simulation of effective thermal conductivity of vapor-filled nanogap and nanocavity, *J. Appl. Phys.* 106 (2009). <https://doi.org/10.1063/1.3186043>.
  - [48] A. De La Escosura-Muñiz, A. Merkoçi, Nanochannels preparation and application in biosensing, *ACS Nano.* 6 (2012) 7556–7583. <https://doi.org/10.1021/nn301368z>.
  - [49] M. Tagliazucchi, I. Szleifer, Theoretical Basis for Structure and Transport in Nanopores and Nanochannels, in: *Chem. Modif. Nanopores Nanochannels*, William Andrew Publishing, 2017: pp. 27–60. <https://doi.org/10.1016/B978-0-323-40182-1.00002-6>.
  - [50] X. Zhang, H. Liu, L. Jiang, Wettability and Applications of Nanochannels, *Adv. Mater.* 31 (2019) 1804508. <https://doi.org/10.1002/adma.201804508>.
  - [51] S. Zhang, F. Xia, S. Demoustier-Champagne, A.M. Jonas, Layer-by-layer assembly in nanochannels: Assembly mechanism and applications, *Nanoscale.* 13 (2021) 7471–7497. <https://doi.org/10.1039/d1nr01113h>.
  - [52] S. Mozaffari, P. Tchoukov, A. Mozaffari, J. Atias, J. Czarnecki, N. Nazemifard, Capillary driven flow in nanochannels – Application to heavy oil rheology studies, *Colloids Surfaces A Physicochem. Eng. Asp.* 513 (2017) 178–187. <https://doi.org/10.1016/j.colsurfa.2016.10.038>.
  - [53] H. Sun, Z. Liu, G. Xin, Q. Xin, J. Zhang, B.Y. Cao, X. Wang, Thermal and flow characterization in nanochannels with tunable surface wettability: A comprehensive molecular dynamics study, *Numer. Heat Transf. Part A Appl.* (2020) 231–251. <https://doi.org/10.1080/10407782.2020.1788849>.
  - [54] H. Singh, R.S. Myong, Critical Review of Fluid Flow Physics at Micro- to Nano-scale Porous

- Media Applications in the Energy Sector, *Adv. Mater. Sci. Eng.* 2018 (2018).  
<https://doi.org/10.1155/2018/9565240>.
- [55] M. Barisik, B. Kim, A. Beskok, Smart wall model for molecular dynamics simulations of nanoscale gas flows, *Commun. Comput. Phys.* 7 (2010) 977–993.  
<https://doi.org/10.4208/cicp.2009.09.118>.
  - [56] L. Qian, C. Tu, F. Bao, Y. Zhang, Virtual-Wall Model for Molecular Dynamics Simulation, *Molecules*. 21 (2016) 1678. <https://doi.org/10.3390/molecules21121678>.
  - [57] M. Barisik, A. Beskok, Molecular dynamics simulations of shear-driven gas flows in nano-channels, *Microfluid. Nanofluidics*. 11 (2011) 611–622. <https://doi.org/10.1007/s10404-011-0827-0>.
  - [58] H. Yasuoka, M. Kaneda, K. Suga, Wall-Adjacent Velocity Profiles of Nano-scale Gas Flows, *J. Stat. Phys.* 165 (2016) 907–919. <https://doi.org/10.1007/s10955-016-1662-1>.
  - [59] M. Barisik, A. Beskok, Equilibrium molecular dynamics studies on nanoscale-confined fluids, *Microfluid. Nanofluidics*. 11 (2011) 269–282. <https://doi.org/10.1007/s10404-011-0794-5>.
  - [60] A.T. Pham, M. Barisik, B. Kim, Molecular dynamics simulations of Kapitza length for argon-silicon and water-silicon interfaces, *Int. J. Precis. Eng. Manuf.* 15 (2014) 323–329. <https://doi.org/10.1007/s12541-014-0341-x>.
  - [61] M. Barisik, A. Beskok, Molecular free paths in nanoscale gas flows, *Microfluid. Nanofluidics*. 18 (2015) 1365–1371. <https://doi.org/10.1007/s10404-014-1535-3>.
  - [62] M. Barisik, A. Beskok, “Law of the nano-wall” in nano-channel gas flows, *Microfluid. Nanofluidics*. 20 (2016) 1–9. <https://doi.org/10.1007/s10404-016-1713-6>.
  - [63] M. Barisik, A. Beskok, Surface-gas interaction effects on nanoscale gas flows, *Microfluid. Nanofluidics*. 13 (2012) 789–798. <https://doi.org/10.1007/s10404-012-1000-0>.
  - [64] B.H. Kim, A. Beskok, T. Cagin, Thermal interactions in nanoscale fluid flow: Molecular dynamics simulations with solid-liquid interfaces, *Microfluid. Nanofluidics*. 5 (2008) 551–559. <https://doi.org/10.1007/s10404-008-0267-7>.
  - [65] R. Rabani, G. Heidarinejad, J. Harting, E. Shirani, Interplay of confinement and density on the heat transfer characteristics of nanoscale-confined gas, *Int. J. Heat Mass Transf.* 126 (2018) 331–341. <https://doi.org/10.1016/j.ijheatmasstransfer.2018.05.028>.
  - [66] R. Rabani, G. Heidarinejad, J. Harting, E. Shirani, Effect of temperature difference between channel walls on the heat transfer characteristics of nanoscale-confined gas, *Int. J. Therm. Sci.* 137 (2019) 13–25.
  - [67] R. Rabani, G. Heidarinejad, J. Harting, E. Shirani, Interplay of wall force field and wall physical characteristics on interfacial phenomena of a nano-confined gas medium, *Int. J. Therm. Sci.* 153 (2020) 106394. <https://doi.org/10.1016/j.ijthermalsci.2020.106394>.
  - [68] R. Rabani, G. Heidarinejad, J. Harting, E. Shirani, Effect of wall stiffness, mass and potential interaction strength on heat transfer characteristics of nanoscale-confined gas, *Int. J. Heat Mass Transf.* 147 (2020) 118929. <https://doi.org/10.1016/j.ijheatmasstransfer.2019.118929>.
  - [69] Heidarinejad Ghassem, Rabani Reza, Shirani Ebrahim, The effect of wall force field on temperature distribution in nanochannel contains Lennard-Jones fluid by molecular dynamic simulation, *Modares Mech. Eng.* 17 (2017) 23–31.
  - [70] R. Rabani, G. Heidarinejad, J. Harting, E. Shirani, Heat Conduction Characteristic of

- Rarefied Gas in Nanochannel, *J. Appl. Fluid Mech.* 13 (2020) 1–13.  
<https://doi.org/10.29252/jafm.13.01.30075>.
- [71] R. Rabani, G. Heidarinejad, J. Harting, E. Shirani, Thermally induced stress in a nanoconfined gas medium, *J. Mol. Model.* 26 (2020) 180.  
<https://doi.org/10.1007/s00894-020-04443-z>.
  - [72] S. Plimpton, Fast Parallel Algorithms for Short-Range Molecular Dynamics, *J. Comput. Phys.* 117 (1995) 1–19. <https://doi.org/10.1006/jcph.1995.1039>.
  - [73] M.S. Daw, M.I. Baskes, Embedded-atom method: Derivation and application to impurities, surfaces, and other defects in metals, *Phys. Rev. B.* 29 (1984) 6443–6453.  
<https://doi.org/10.1103/PhysRevB.29.6443>.
  - [74] F.H. Stillinger, T.A. Weber, Computer simulation of local order in condensed phases of silicon, *Phys. Rev. B.* 31 (1985) 5262–5271. <https://doi.org/10.1103/PhysRevB.31.5262>.
  - [75] M.P. Allen, D.J. Tildesley, J.R. Banavar, Computer Simulation of Liquids, *Phys. Today.* 42 (1989) 105–106. <https://doi.org/10.1063/1.2810937>.
  - [76] J.H. Irving, J.G. Kirkwood, The Statistical Mechanical Theory of Transport Processes. IV. The Equations of Hydrodynamics, *J. Chem. Phys.* 18 (1950) 817–829.  
<https://doi.org/10.1063/1.1747782>.
  - [77] B.D. Todd, P.J. Davis, D.J. Evans, Heat flux vector in highly inhomogeneous nonequilibrium fluids, *Phys. Rev. E.* 51 (1995) 4362–4368.  
<https://doi.org/10.1103/PhysRevE.51.4362>.
  - [78] J. Sun, Z.X. Li, Effect of gas adsorption on momentum accommodation coefficients in microgas flows using molecular dynamic simulations, *Mol. Phys.* 106 (2008) 2325–2332.  
<https://doi.org/10.1080/00268970802452020>.
  - [79] F. Bao, Y. Huang, L. Qiu, J. Lin, Applicability of molecular dynamics method to the pressure-driven gas flow in finite length nano-scale slit pores, *Mol. Phys.* 113 (2015) 561–569. <https://doi.org/10.1080/00268976.2014.960495>.
  - [80] P.A. Tipler, R.A. Llewellyn, *Modern Physics*, W.H. Freeman, New York, 2007.  
<https://doi.org/10.1017/CBO9781107415324.004>.
  - [81] C.Y. Ho, R.W. Powell, P.E. Liley, Thermal Conductivity of the Elements: A Comprehensive Review, Vol. 3, Suppl. No 1, *J. Phys. Chem. Ref. Data.* 3 (1974).  
<http://www.dtic.mil/docs/citations/ADD095039> (accessed August 24, 2019).
  - [82] N. Asproulis, D. Drikakis, Boundary slip dependency on surface stiffness, *Phys. Rev. E - Stat. Nonlinear, Soft Matter Phys.* 81 (2010) 1–5.  
<https://doi.org/10.1103/PhysRevE.81.061503>.
  - [83] N. Asproulis, D. Drikakis, Wall-mass effects on hydrodynamic boundary slip, *Phys. Rev. E - Stat. Nonlinear, Soft Matter Phys.* 84 (2011) 031504.  
<https://doi.org/10.1103/PhysRevE.84.031504>.
  - [84] E.W. Lemmon, R.T. Jacobsen, Viscosity and thermal conductivity equations for nitrogen, oxygen, argon, and air, *Int. J. Thermophys.* 25 (2004) 21–69.  
<https://doi.org/10.1023/B:IJOT.0000022327.04529.f3>.
  - [85] W.M. Trott, J.N. Castañeda, J.R. Torczynski, M.A. Gallis, D.J. Rader, An experimental assembly for precise measurement of thermal accommodation coefficients, *Rev. Sci. Instrum.* 82 (2011) 035120. <https://doi.org/10.1063/1.3571269>.
  - [86] Pinki, P. Kulkarni, D.S. Sundaram, First-Principles Informed Atomistic-Scale Calculations of

- Equilibrium Energy Accommodation Coefficients for Aluminum-Noble Gas Systems, *J. Phys. Chem. C.* 124 (2020) 7182–7195. <https://doi.org/10.1021/acs.jpcc.9b11394>.
- [87] H. Heinz, R.A. Vaia, B.L. Farmer, R.R. Naik, Accurate simulation of surfaces and interfaces of face-centered cubic metals using 12-6 and 9-6 lennard-jones potentials, *J. Phys. Chem. C.* 112 (2008) 17281–17290. <https://doi.org/10.1021/jp801931d>.
- [88] R. Bhadauria, N.R. Aluru, A quasi-continuum hydrodynamic model for slit shaped nanochannel flow, *J. Chem. Phys.* 139 (2013) 074109. <https://doi.org/10.1063/1.4818165>.
- [89] G. Munaò, A. Correa, A. Pizzirusso, G. Milano, On the calculation of the potential of mean force between atomistic nanoparticles, *Eur. Phys. J. E.* 41 (2018) 1–9. <https://doi.org/10.1140/epje/i2018-11646-3>.
- [90] B.H. Kim, Interface thermal resistance modeling of the silicon-argon interface, *Int. J. Precis. Eng. Manuf.* 14 (2013) 1023–1028. <https://doi.org/10.1007/s12541-013-0137-4>.